Strengthening Mechanisms in NiAl Bronze: Hot Deformation by Rolling and Friction-Stir Processing

SARATH K. MENON, FRANK A. PIERCE, BRIAN P. ROSEMARK, KEIICHIRO OH-ISHI, SRINIVASAN SWAMINATHAN, and TERRY R. MCNELLEY

Microstructures produced by isothermal hot rolling of a NiAl bronze material were evaluated by quantitative microscopy methods and parameters describing the contributions of precipitate dispersions, grain size, solute content, and dislocation density to the yield strengths of the individual constituents of microstructure were determined. Models for the strengths of the individual constituents were combined to predict the temperature dependence of the yield strength as a function of hot rolling temperature, and the prediction was found to be in good agreement with measured yield strengths. The models were applied to microstructures in a stir zone produced by multipass friction-stir processing (FSP) and, again, found to predict measured yield strengths with high accuracy. Such models may aid in assessing the role of microstructure gradients produced during FSP and other processes.

DOI: 10.1007/s11661-012-1181-x

I. INTRODUCTION

GRADIENTS in strain, strain rate, and temperature during deformation processing may lead to gradients in microstructure that, in turn, affect material response during subsequent mechanical testing of as-processed material. Assessing the role of such gradients in mechanical response can be facilitated by microstructure-based models of strength, especially when gradients are steep or when such gradients are an inherent feature of the deformation technique. The latter is the case for friction-stir processing (FSP), which is an allied technique of friction stir welding (FSW), a solid-state joining method developed at The Welding Institute.[1–3] In FSP, a rotating, nonconsumable cylindrical tool with a concentric projecting pin is pressed into a work piece surface. A combination of frictional and adiabatic heating leads to formation of a plasticized column of material around the pin as it penetrates the surface. When the tool shoulder contacts the work piece surface the tool may be traversed across the surface to process the volume of material that is swept by the pin profile. This volume of material is termed the stir zone (SZ). The FSP thermomechanical cycle includes rapid transients as well as steep gradients in strain, strain rate, and temperature. Accordingly, there are gradients in microstructures and mechanical properties within the SZ and, especially, outward into the surrounding base material.[3–5]

The application of FSP to as-cast NiAl bronze materials results in simultaneous increases in both tensile strength and ductility in the SZ material.[6,7] However, reduced ductility has been observed when the deforming gage sections of tensile samples include regions of inhomogeneous microstructure. Such reduced ductility may reflect strain localization but could also be caused by other processing-related defects, such as inclusions or inadequate bonding of stir zone to base material.[6,7] The latter may occur on the advancing side of the tool, *i.e.*, on the side where tool traversing and rotation speeds are additive and where gradients in microstructure are especially steep. Microstructure gradients on the retreating side of the tool, where tool traversing and rotation speeds subtract, generally are more gradual.[3–5]

Microstructure-based models of strength established from isothermal and uniform annealing or deformation studies can incorporate alloy constitution, constituent and phase morphologies, and grain sizes. The solute content of each phase, the presence of various dispersions, and the state of strain hardening in the material are affected by the thermomechanical history. Recent analytical microscopy investigations of the SZ and surrounding microstructures following FSP of NiAl bronze have shown that local peak temperatures can be estimated if it is assumed that concurrent deformation accelerates SZ phase transformations.[8,9] Also, strains in the thermomechanically affected zone (TMAZ) surrounding the SZ can be estimated by evaluating the shape change of microstructure constituents.[10] Nevertheless, the rapid transients and steep gradients within

SARATH K. MENON, Research Professor, and TERRY R. McNELLEY, Distinguished Professor, are with the Department of Mechanical and Aerospace Engineering, Naval Postgraduate School, 700 Dyer Road, Monterey, CA 93943-5146. Contact e-mail: tmcnelley@nps.edu FRANK A. PIERCE, formerly Student, with the Department of Mechanical and Aerospace Engineering, Naval Postgraduate School, is now Engineer Officer, with United States Coastguard, CGS STRATTON, Alameda, CA. BRIAN P. ROSEMARK, formerly Student, with the Department of Mechanical and Aerospace Engineering, Naval Postgraduate School, is now with the NUWCDIVNPT, Code 3423, Newport, RI. KEIICHIRO OH-ISHI, Associate Professor, is with the Nagaoka University of Technology, 1603-01 Kamitomioka, Nagaoka 940-2188, Japan. SRINIVASAN SWAMINATHAN, Research Scientist, is with General Electric Global Research, Bangalore 560066, India.

Manuscript submitted August 17, 2011.
Article published online May 17, 2012

the SZ, within the TMAZ, and into the base metal preclude direct correlation of the FSP thermomechanical cycle with local details of the microstructure, *e.g.*, composition as well as grain size. However, annealing alone or uniform deformation under isothermal conditions will enable separate characterization of temperature and strain effects on the details of microstructure of the NiAl bronze material of the current investigation. The alloy constitution and phase transformations will be reviewed and the scope of the experiments leading to development of a microstructure-based model for this material will be outlined in the remainder of this section.

This NiAl bronze alloy conforms to UNS95800, and its composition is nominally Cu-9.5Al-5Ni-4Fe (wt pct).[11–13] The alloy constitution and transformation characteristics in the as-cast condition and after FSP have been discussed in detail elsewhere.[6,8,9,14–23] Briefly, solidification occurs at ≈1326 K (≈1050 °C) with the formation of a body-centered cubic β phase. During slow cooling at a rate on the order of $\approx 10^{-3}$ °C s^{-1}, which is typical of many large cast marine components fabricated in this alloy, the primary α face-centered cubic (fcc) terminal solid solution begins to form in the β as temperature decreases below approximately 1273 K (1000 °C). The primary α forms with a Widmannstätten morphology. Globular κ_{ii} particles, which are nominally Fe_3Al with a DO_3 structure, begin to precipitate in the remaining β at approximately 1203 K (930 °C) while finer κ_{iv} particles, which are also Fe_3Al, start to form in the primary α at approximately 1133 K (860 °C). During cooling, the volume fraction of β decreases approximately linearly with temperature below ≈1273 K (≈1000 °C) until the eutectoid decomposition reaction $\beta \rightarrow \alpha + \kappa_{iii}$ occurs over the temperature range of 1073 K to 1033 K (800 °C to 760 °C). The κ_{iii} is nominally NiAl, has a B2 structure, and it forms initially as an epitaxial layer on the globular κ_{ii} at the onset of the eutectoid reaction. Thus, as-cast NiAl bronze microstructures comprise elongated, approximately ellipsoidal primary α grains, roughly 175 μm × 425 μm in size, embedded in a coarse lamellar eutectoid constituent. The finer κ_{iv} particles in the primary α vary in size up to 5 μm, whereas the globular κ_{ii} composite particles are typically 10 to 20 μm in diameter; the outer κ_{iii} epitaxial layer on the globular κ_{ii} is generally 1 to 5 μm in thickness.

The characteristics of SZ and TMAZ microstructures also have been described in detail elsewhere.[6,8,9,23] Essentially, peak SZ temperatures are in the range 1073 K to 1273 K (800 °C to 1000 °C), and corresponding microstructures consist of various mixtures of deformed primary α that has not transformed, as well as transformation products of the β formed during heating and deformation.[10,24] The κ_{iv} particles precipitated during slow cooling of the as-cast materials are highly refined in the SZ primary α, suggesting that the κ_{iv} dissolves when local temperatures exceeds 1133 K (860 °C) during FSP and then reprecipitated during subsequent cooling. The primary α grains typically are equiaxed but vary in size from <1 to >10 μm in size depending on SZ location and processing conditions. The presence of undissolved κ_{ii} in some portions of the SZ indicates that local temperatures were below 1203 K (930 °C) in such regions. Transformation products of deformation-induced β generally comprise fine Widmannstätten α and refined lamellar or bainitic transformation products of the β. In some SZ and surrounding TMAZ locations, martensitic transformation products of the β have been observed. The SZ microstructures in material subjected to a single FSP traverse are generally inhomogeneous. In contrast, FSP involving overlapping passes during processing of large areas generally results in more homogeneous SZ microstructures that comprise refined and equiaxed α grains embedded in transformation products of β.

In the current investigation, isothermal hot rolling involving heating and rolling with reheating between successive passes was conducted at temperatures up to 1273 K (1000 °C). A quantitative analysis of the resulting microstructures was conducted and tensile properties were determined. Models including solute, grain size, dispersion, and dislocation contributions were developed and applied to the microstructures produced by the hot-rolling experiments. In turn, these models were correlated with observed distributions of yield strength for a material subjected to multipass FSP.

II. EXPERIMENTAL PROCEDURES

The NiAl bronze materials of this investigation were acquired as plates approximately 40 × 20 × 4cm^3 in size that had been machined from large marine castings. Chemical analyses were conducted by Anamet, Inc. (Hayward, CA) on these materials and the resulting composition data for the two materials examined in the current work are given included in Table I.

Billets for hot rolling were machined from the plate designated alloy 1 in Table I. Billet dimensions were either 110 mm × 40 mm × 10 mm or 55 mm × 40 mm × 30 mm, depending on the intended strain. The billets were heated and equilibrated at the intended rolling temperature, which was in the range of 1143 K to 1273 K (870 °C to 1000 °C), in a Blue-M box-type furnace. Hot rolling was carried out using a laboratory rolling mill and manual adjustment of the roll gap to obtain an approximate reduction of 10 pct on each successive pass. Billet temperature was maintained by reequilibrating at the rolling

Table I. Composition Data (Weight Percent) for NiAl Bronze (UNS95800)

Element	Cu	Al	Ni	Fe	Mn	Si	Pb
Minimum to maximum	(minimum) 79.0	8.5 to 9.5	4.0 to 5.0	3.5 to 4.5	0.8 to 1.5	0.10 (maximum)	0.03 (maximum)
Nominal	81	9	5	4	—	—	—
Alloy 1	79.26	9.80	4.71	4.95	1.01	0.08	0.01
Alloy 2	81.3	9.17	4.46	3.68	1.24	0.06	<0.005

temperature between each successive pass. The thicker starting billets were rolled to a total equivalent strain of 2.3 (a reduction of 10:1), and the thinner starting billets were rolled to an equivalent strain of 1.2 (a reduction of 3.5:1) while maintaining the longest billet dimension as the rolling direction. At the conclusion of the final pass, the rolled material was allowed to cool in air to room temperature. Anneals 1 hour in duration in the absence of deformation were conducted at selected temperatures in the range of 1073 K to 1273 K (800 °C to 1000 °C) and involved rectangular coupons nominally 2.5 mm in thickness. After completion of annealing, these coupons were removed from the furnace and allowed to cool in laboratory air.

Sheet-type tensile testing coupons were sectioned from as-rolled materials by wire electric discharge machining (EDM) using a Charmilles–Andrew EDM (Agie Charmilles Ltd., Coventry, UK). The gage section dimensions were 15 × 6.35 × 2.5 mm with a 6.35 mm radius of curvature into the sample shoulder. All sample surfaces were lightly ground to remove any residual machining damage prior to tension testing. Constant extension rate tests were conducted to failure using a crosshead speed corresponding to a nominal strain rate of 10^{-3}seconds^{-1}. Microhardness testing of the hot-rolled materials was conducted using a Buehler Micromet 2004 (Buehler, Lake Bluff, IL) with a diamond pyramid indenter and a load of 100 g. The samples for microhardness testing of rolled material were sectioned to reveal the RD/ND plane (RD is the rolling direction, ND is the normal direction to the rolling plane, and TD is the transverse direction). After metallographic preparation (described in the subsequent discussion), 20 microhardness measurements were made in a traverse along the ND and the microstructure constituent (primary α or β-phase transformation products) in which each microhardness indentation was located was recorded.

The details of the FSP procedures of concern in the current investigation have been given in previous reports.[6,8–10,23,24] Briefly, multipass FSP was conducted using tools designed with a pin in the shape of a truncated cone and fabricated in Densimet 176. The tool shoulder diameter was 28.6 mm, the pin base diameter was 15 mm, the length was 12.7 mm, and tip diameter was 6.3 mm. The pin design also included a stepped spiral feature. FSP was conducted at a tool rotation rate of 1000 rpm and traversing rate of 76 mm min^{-1}. The NiAl bronze plates were clamped to the machine anvil and the initial traverse was along the centerline of the plate and parallel to the long edge of the plate. Multipass processing followed a rectangular spiral pattern with the advancing side of the tool to the outside of the spiral pattern and a step-over distances between adjacent passes of 4.5 mm to achieve complete overlap of the pin profile on successive passes. FSP was conducted over an area approximately 25 × 15 cm^2 in size. Tool plunge force was initially ≈29 kN and decreased to ≈18 to 22 kN as the plate heated during the processing.

After FSP, miniature sheet-type tensile coupons having gage sections 15.9 mm in length, 1.7 mm in width, and approximately 1 mm in thickness were machined using the wire EDM system. To obtain mechanical property data as a function of depth, a blank with the shape of the gage section was sectioned from the full thickness of the as-friction-stir processed material. Then, this blank was carefully sectioned to provide the individual tensile coupons 1 mm in thickness, beginning at the plate surface that had been in contact with the tool. As each coupon was sectioned, the depth of the coupon center relative to the plate surface was determined by a measurement of the remaining blank thickness. Again, constant extension rate tests were conducted to failure using a crosshead speed corresponding to a nominal strain rate of 10^{-3} seconds^{-1}.

Metallographic examination of as-received, annealed, hot-rolled, and friction-stir processed materials all involved optical microscopy, scanning electron microscopy (SEM), and scanning transmission electron microscopy (STEM) methods. Orientation imaging microscopy (OIM) methods were also employed in characterization of the NiAl bronze microstructures. Energy-dispersive spectroscopy (EDS) methods were employed during SEM examination to obtain composition data for various microstructure constituents. The samples for microstructural examination were prepared by standard metallographic techniques and finally electropolished using an electrolyte containing 30 pct nitric acid in methanol cooled to ≈–268 K (≈–5 °C) at 15 V. A Zeiss Neon 40 field emission scanning electron microscope (Carl Zeiss, Oberkochen, Germany) operating at 20 kV was used for all imaging work and the EDAX Hikari camera system (EDAX, Inc., Draper, UT) was used for orientation imaging. EDS work was carried out with the Apollo 10 SDD detector and data analyzed using the Genesis software from EDAX. STEM imaging was obtained at 30kV in the same microscope.

III. RESULTS

A. *The Effect of Hot Rolling on NiAl Bronze Microstructure*

Representative microstructures of the as-cast NiAl bronze material of this investigation are shown in the backscattered electron micrographs presented in Figure 1. In Figure 1(a), a lamellar constituent formed by the eutectoid decomposition reaction $\beta \rightarrow \alpha + \kappa_{iii}$ during cooling surrounds elongated but irregularly shaped grains of the primary α. Coarse, globular particles distributed mainly in the eutectoid constituent are the κ_{ii} (Fe_3Al) phase formed in the β during cooling through temperatures above the eutectoid. A finer dispersion of the κ_{iv} (Fe_3Al) particles is apparent in the primary α constituent. At a higher magnification in Figure 1(b), the lamellar morphology of the κ_{iii} (NiAl) phase is shown more distinctly. The κ_{iii} lamella are typically ≈1.0 μm in thickness, although in some locations, the lamellar morphology of the κ_{iii} apparently gives way to a particulate form during transformation of the β. In Figure 1(b), the κ_{iii} seems to have formed epitaxially on the κ_{ii} prior to the onset of the eutectoid decomposition of the β. Also, the finer κ_{iv} particles exhibit both equiaxed and cruciform morphologies. These particles are typically ≤1.0 μm in size.

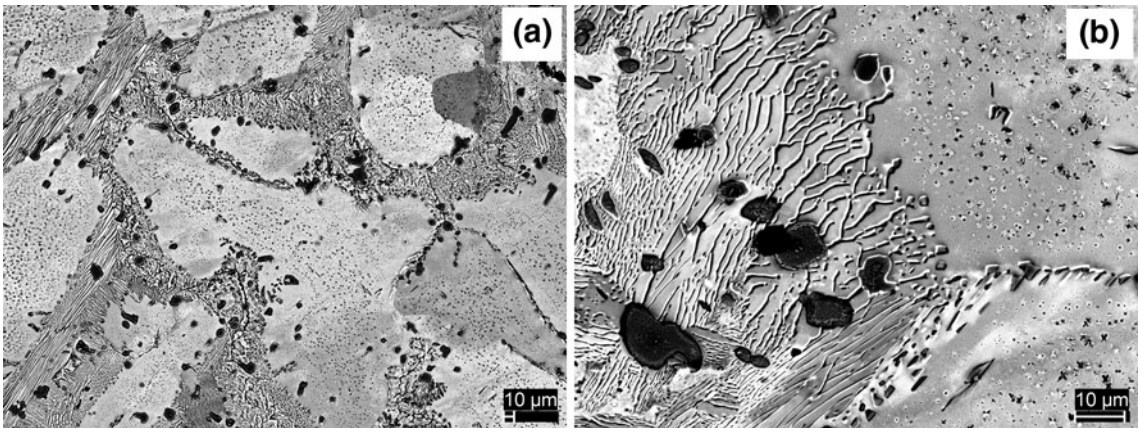

Fig. 1—Backscatter electron images from as-cast NiAl bronze material showing (*a*) the coarse primary α and eutectoid transformation product of β. Coarse, globular κ_{ii} (Fe_3Al) particles are apparent throughout the eutectoid constituent whereas fine κ_{iv} (also Fe_3Al) may be observed in the primary α. Details of the lamellar nature of the eutectoid constituent are shown at higher magnification in (*b*). Epitaxial formation of κ_{iii} (NiAl) on the κ_{ii} may also be discerned in this image.

Microstructures resulting from annealing alone or from isothermal hot rolling of alloy 1 at various temperatures above the temperature of the eutectoid reversion reaction $\alpha + \kappa_{iii} \rightarrow \beta$ are shown in the optical micrographs of Figure 2. Equilibration of small samples at the annealing temperature followed by air cooling results in refined transformation products of the β as shown in Figure 2(a). The coarse lamellar eutectoid formed in the very slowly cooled as-cast material (Figure 1) is no longer apparent. After cooling from the highest temperature in this study (1273 K [1000 °C]), the β formed by the eutectoid reversion retransforms on cooling to a mixture of α, with a distinct Widmanstätten morphology, and a dark-etching constituent in optical micrographs. Cooling after equilibration at 1223 K (950 °C) results in finer Widmanstätten α embedded in the dark-etching constituent and cooling after equilibration at still lower temperatures results in further refinement of the cooling transformation products of the β.

Deformation of both the primary α and the β that was formed by the eutectoid reversion apparently takes place in a compatible manner during isothermal hot rolling so that the shape changes of the primary α and the transformation products of the β reflect the rolling reduction (an equivalent strain of 1.2 in Figure 2(b) and 2.3 in Figure 2(c)). The formation of equiaxed grains within the primary α as well as refinement of the Widmanstätten α within the β transformation products are both evident in the microstructures of materials hot rolled at 1273 K (1000 °C). An examination of Figures 2(b) and (c) reveals that these constituents of the microstructure become finer as the isothermal rolling temperature is reduced, while the relative fraction of the primary α increases at the expense of the β phase transformation products.

The backscatter electron images in Figure 3 provide more details of the microstructures produced during hot rolling to an equivalent strain of 2.3 at either 1223 K (950 °C) (Figure 3(a)) or at 1273 K (1000 °C) (Figure 3(b)). These images also highlight the compatible deformation of the primary α and the β phases during deformation. Refined Widmanstätten α is apparent within the β transformation products for both of these processing temperatures. From a previous work, these transformation products also include bainitic and lamellar products of β decomposition. Of particular note in Figure 3 is the presence of refined and equiaxed grains within the elongated primary α constituent. The primary α constituent has become elongated in the rolling direction and compressed in the direction normal to the rolling plane. Nevertheless, the individual grains within this constituent are equiaxed and contain well-defined annealing twins with straight boundaries. In some locations, the primary α seems to have been reduced to a thickness equivalent to the recrystallized grain size in the direction normal to the rolling plane.

The relative volume fractions of untransformed primary α and β transformation products were determined by quantitative microscopy methods applied to alloy 1 material subjected to annealing alone or to isothermal hot rolling at various temperatures. The results of this analysis are included in Table II and plotted as functions of temperature in Figure 4.

These data exhibit a linear temperature dependence of the volume fraction of β transformation products coinciding with that reported previously for various materials corresponding to the composition limits cited in Table I. Extrapolation to zero volume fraction β transformation products suggests that the onset of the eutectoid reversion reaction $\alpha + \kappa_{iii} \rightarrow \beta$ occurs at approximately 1053 K (780 °C).

B. *Mechanical Properties of the Hot-Rolled Material*

Mechanical property data for the materials of Figure 2 are summarized in Figures 5 and 6. The results of Vickers microhardness testing in hot-rolled materials are presented in Figure 5(a). The data are plotted separately according to the measurements made in either the primary α or the β-phase transformation products. Data were acquired for materials rolled to equivalent strains of either 1.2 or 2.3 for each of the rolling temperatures. These data show that the β transformation products are always harder when

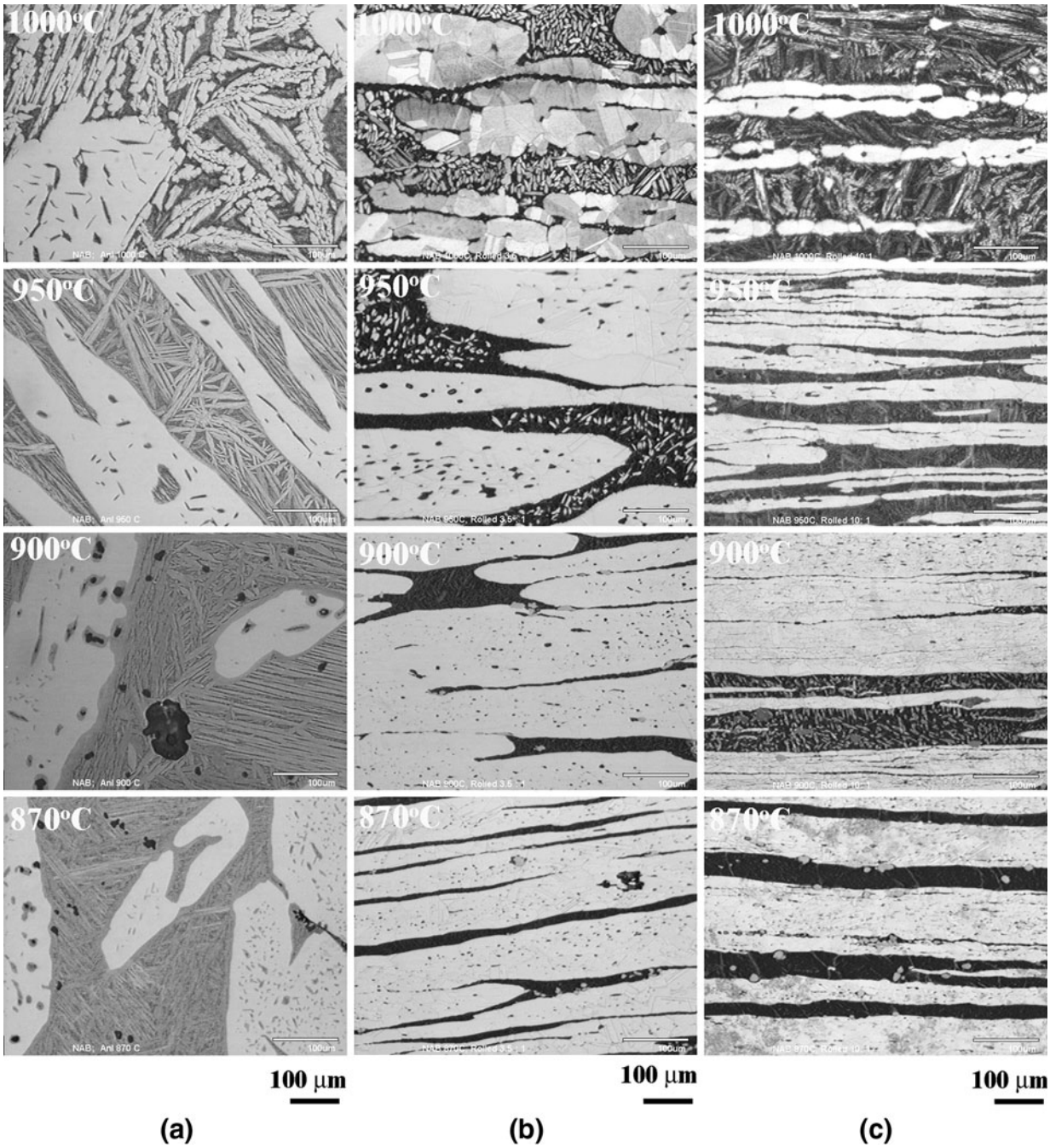

Fig. 2—Optical micrographs of the as-cast NiAl bronze materials after various thermomechanical treatments at the indicated temperatures. (*a*) The samples have been subjected to annealing followed by air cooling. (*b*) The samples have been subjected to isothermal hot rolling to a reduction of 3.5:1, corresponding to an equivalent strain of 1.2. (*c*) The samples have been subjected to isothermal hot rolling to a reduction of 10:1, corresponding to an equivalent strain of 2.3.

compared with the primary α although both constituents soften as the isothermal hot-rolling temperature is increased. An examination of these data also reveals that the both constituents soften as the equivalent rolling strain is increased. The average value of the 20 microhardness measurements from each sample is compared in Figure 5(b) to the volume-fraction weighted average microhardness obtained by combining the data of Figures 4 and 5(a). That these plots coincide is not surprising, but it is noteworthy that these data suggest that these materials become harder as the rolling temperature increases. This result reflects the increasing volume fraction of the harder β constituent as the rolling temperature increases.

A more complex pattern of behavior is observed in Figure 6 in the tension test data acquired from as-cast as well as annealed and hot-rolled materials. Tension test results for the as-cast material are included in these graphs, and the minimum and maximum as well as mean values are indicated for each property. Also in

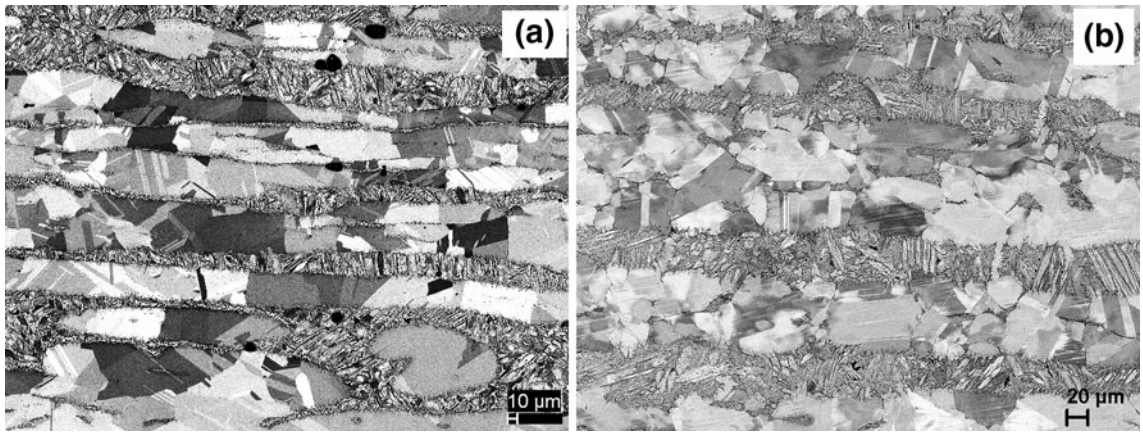

Fig. 3—Backscatter electron images showing refinement of the grain size in the primary α and refined transformation products of the β after isothermal hot rolling at (*a*) 950 °C and (*b*) 1000 °C. Annealing twins are apparent in both (*a*) and (*b*); a refined Widmanstätten α morphology may be discerned in the β transformation products in both (*a*) and (*b*).

Table II. Measured Microstructure Parameters for Each Isothermal Hot Rolling Temperature (Alloy 1)

Isothermal Rolling Temperature K (°C)	V_α (pct)	d_α (μm)	Size (Spacing) of κ_{iii} in β (nm)	Size and (Spacing) of κ_{iv} in α (nm)
1273 (1000)	16.8	51.4	645 (885)	90 (950)
1223 (950)	45.0	40.5	768 (1221)	—
1173 (900)	63.4	28.5	351 (708)	263 (1740)
1143 (870)	86.0	21.4	220 (531)	257 (1000)

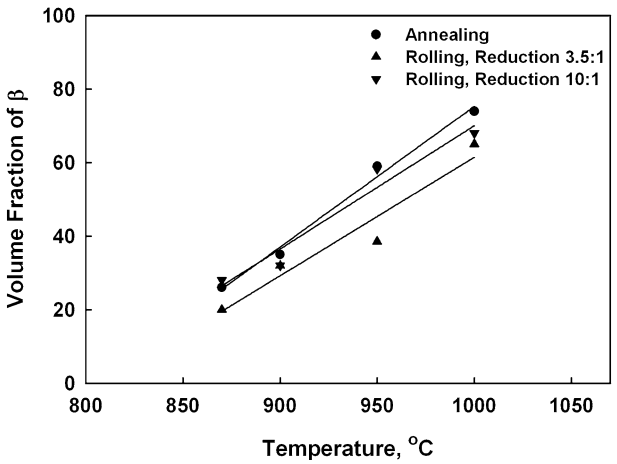

Fig. 4—A graph of the volume fraction of β transformation products (from optical micrographs as in Fig. 2) as a function of the isothermal hot-rolling temperature shows that the volume fraction of β varies linearly with temperature after either isothermal annealing or hot rolling.

Figure 6, yield and ultimate tensile strengths as well as ductility are plotted as functions of the annealing or hot-rolling temperature for these materials. An inspection of these data reveals that isothermal hot rolling increases the yield and ultimate tensile strengths and simultaneously increases tensile ductility, especially at the highest rolling temperatures. Annealing at progressively higher temperatures in the absence of rolling deformation resulted in small increases in both yield and ultimate tensile strengths, whereas tensile ductility remained in the range of 5 to 6 pct elongation to failure and ductility after annealing was lower than that of the as-cast material. In contrast, materials subjected to isothermal hot rolling exhibited a general trend toward lower yield strengths as the rolling temperature was increased. Ultimate tensile strengths were nearly constant for materials rolled to an equivalent strain of 1.2 but increased for materials rolled to an equivalent strain of 2.3. The combination of a decreasing yield and increasing ultimate strength as functions of isothermal hot-rolling temperature reflects the pronounced increase in tensile ductility in materials rolled to an equivalent strain of 2.3. Indeed, these ultimate tensile strength data mirror the temperature dependence of the average microhardness for this alloy shown in Figure 5(b). Nevertheless, direct application of the correlation $H_V \approx 3\sigma_{UTS}$, where H_V is the Vickers hardness and σ_{UTS} is the ultimate tensile strength, is not appropriate because the tensile ductility varies greatly over the range of temperature investigated.

C. *Strengthening Mechanisms*

At ambient temperature the constituents of microstructure in these NiAl bronze materials comprise Cu-base fcc solid solutions with various dispersed phases. Refined grain structures reflect recrystallization associated with hot deformation, and recovery after deformation would be expected to result in the presence of dislocation substructures. Thus, the operative strengthening mechanism in these materials would be

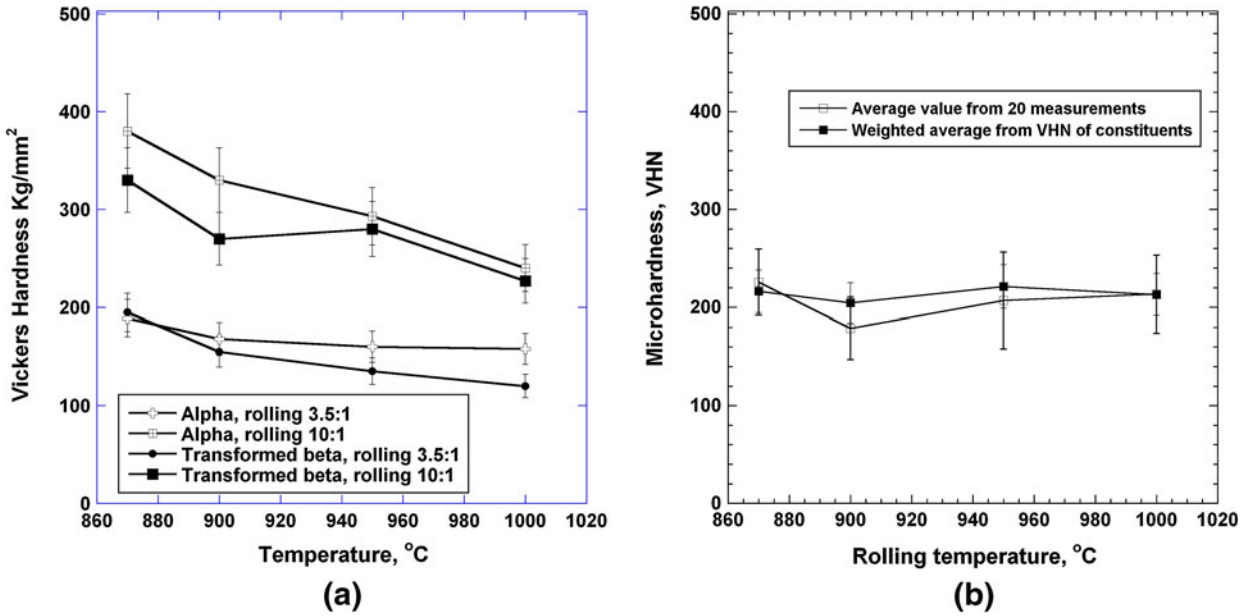

Fig. 5—In (*a*), Vickers microhardness is plotted as a function of temperature for NiAl bronze subjected to annealing alone or to isothermal hot rolling. The average values of the microhardness, determined from 20 microhardness measurements and the volume-fraction weighted average from microhardness data for the individual constituents, are plotted as a function of temperature in (*b*).

expected to include solid-solution hardening, dispersion effects, grain size strengthening, and strain hardening. Furthermore, the contributions of each of these mechanisms will be different in the primary α and the β transformation products.

Figure 7 shows microstructures at a higher resolution after hot rolling at 1273 K (1000 °C) to an equivalent strain of 2.3. The image in Figure 7(a) was obtained in the cooling transformation products of the β and shows highly refined, lamellar $\alpha + \kappa_{iii}$ intermingled with a bainitic transformation product. Both of these constituents also contain fine, globular κ_{ii} approximately 300 nm in size, *i.e.*, much finer than the globular κ_{ii} in the as-cast material (Figure 1). The primary α constituent exhibits a very fine dispersion of κ_{iv} particles, as illustrated in the image of Figure 4(b). The sizes and spacings of these dispersed particles were evaluated for each rolling temperature, and the results are summarized in Table II. It is noteworthy that the fine κ_{iv} dispersion observed in material rolling at 1273 K (1000 °C) was not present at 1223 K (950 °C). Apparently, the Fe dissolved after heating and deformation at the lower temperature did not reprecipitate. In contrast, at least some of the κ_{iv} dispersion in the as-cast condition did dissolve at lower rolling temperatures and experienced refinement during deformation.

The OIM data acquired from as-cast material and materials subjected to isothermal hot rolling either at 1273 K (1000 °C) or 1173 K (900 °C) are shown in Figure 8 as inverse pole figure (IPF) grain maps and corresponding grain-to-grain misorientation distributions. In all cases, these maps present orientation data for the face-centered cubic Cu solid solution. Kikuchi patterns from the various κ-phases were not indexed and the corresponding locations from which such patterns were obtained are coded in black in the grain maps. A representative IPF map from the as-cast material shows only portions of several grains in the field of view presented in Figure 8(a). A comparison of this image with the microstructures in Figure 1 reveals that the dispersed, particulate nature of the finer κ_{iv} and coarser κ_{ii} phases is captured in this OIM micrograph. However, the lamellar κ_{iii} phase in the eutectoid constituent (*i.e.*, as shown in Figure 1(b)) appears more nearly particulate in Figure 8(a). This reflects that the step size used in the OIM analysis is on the order of the thickness of the κ_{iii} lamella and is too large to capture fully the morphology of this phase. The uniform grain contrast within the Cu phase indicates that there is little lattice curvature within the α-phase grains although the misorientation distribution in Figure 8(b) includes a population of low-angle boundaries (misorientation ≤5 deg). There are also 60 deg boundaries in the distribution. Otherwise, the misorientation distribution is approximately that predicted by Mackenzie[25] for randomly oriented cubes.

An IPF map from the material subjected to isothermal hot rolling at 1273 K (1000 °C) is shown in Figure 8(c) and illustrates refinement to a mean linear intercept grain size of 51.4 μm (these data are also summarized in Table II). The various κ phases apparently have been redistributed into elongated stringers aligned with the rolling direction (vertical in the images of Figures 8(c) and (e)). Of particular note in Figures 8(c) and (e) is the presence within almost all grains of the straight boundaries of annealing twins characteristic of well-annealed Cu. Indeed, the relative population of 60 deg boundaries in the misorientation distributions (Figures 8(d) and (f)), greatly exceeds that expected in the Mackenzie distribution, and detailed analysis of the OIM data revealed that these boundaries are predominantly first-order twin interfaces. There is also a population of low-angle (≤5 deg) boundaries,

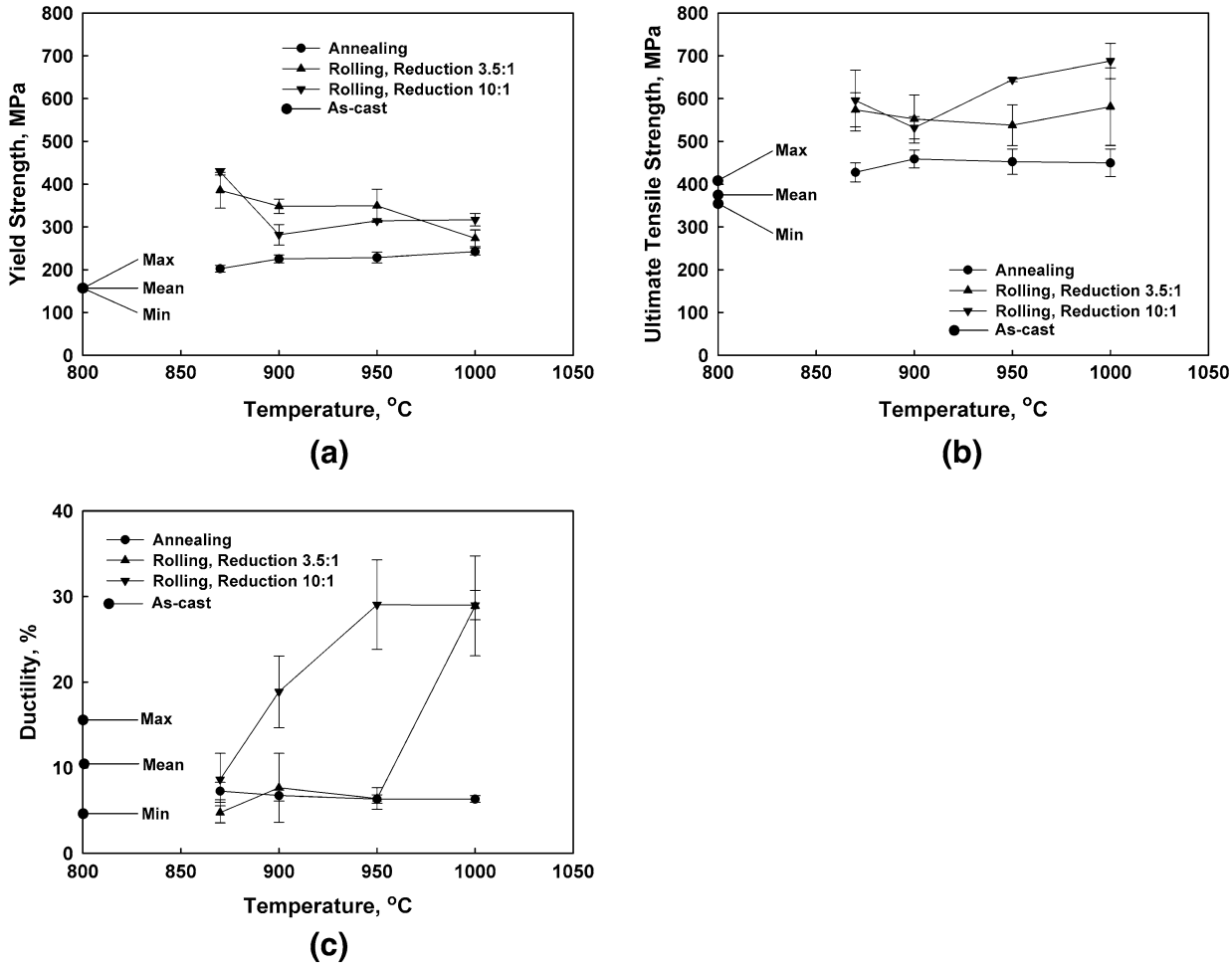

Fig. 6—Ambient temperature yield strength (*a*), ultimate tensile strength (*b*), and tensile ductility (*c*), are plotted as a function of annealing or isothermal hot-rolling temperature for tensile samples subjected to annealing alone or to isothermal hot rolling to different strains. Corresponding data for as-cast material are included on each graph.

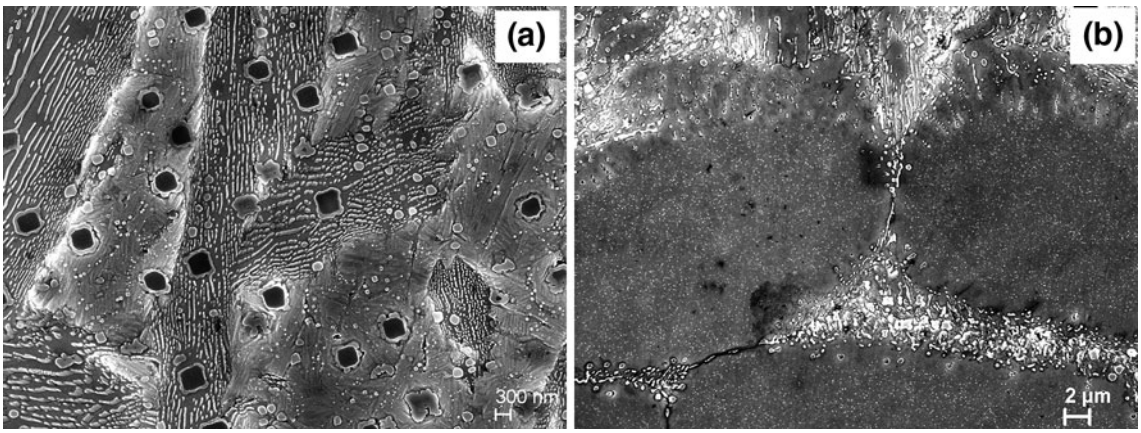

Fig. 7—Secondary electron images show the fine structure within the β transformation products in (*a*) and within the primary α in (*b*). Fine κ phases as well as lamellar and bainitic products have formed in the β transformation products, whereas fine κ precipitate dispersions are apparent in the primary α.

whereas the remainder of the misorientation distribution closely approximates the Mackenzie[25] distribution with a peak near 40 deg. Hot rolling at a lower temperature of 1173 K (900 °C) resulted in a finer grain size (≈28.5 μm), but annealing twins are still apparent and the relative population of 60 deg boundaries is the same

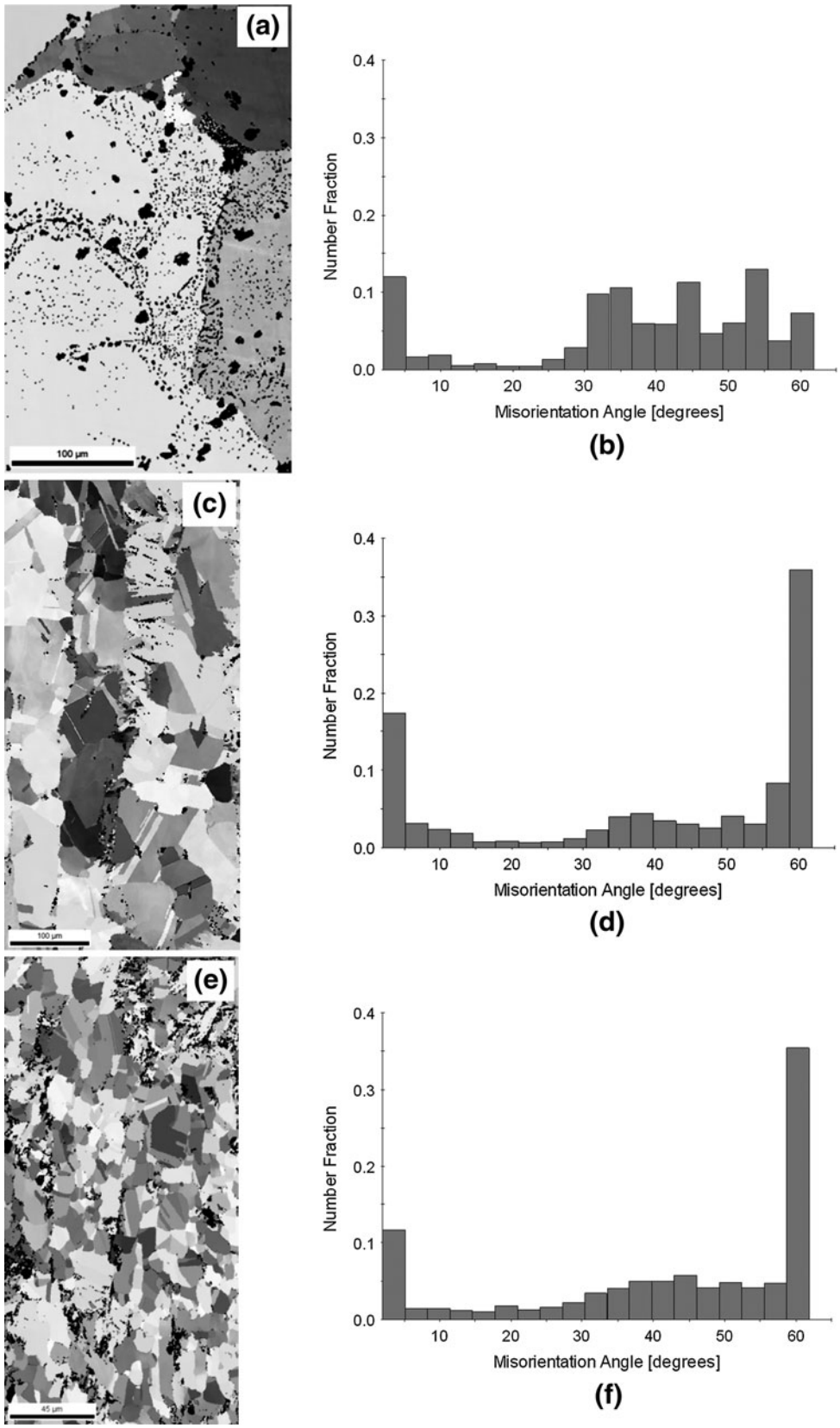

Fig. 8—Orientation imaging microscopy results in the form of inverse pole figure maps and misorientation distributions from as-cast material: (*a*) and (*b*) material hot rolled at 1000 °C, (*c*) and (*d*) and material hot rolled at 900 °C, and (*e*) and (*f*) show the coarse grain structure in as-cast material and that grain refinement in the primary α depends on the deformation temperature. The presence of annealing twins in hot-rolled material is confirmed by the presence of a large population of 60 deg boundaries in the misorientation distributions for hot-rolled materials.

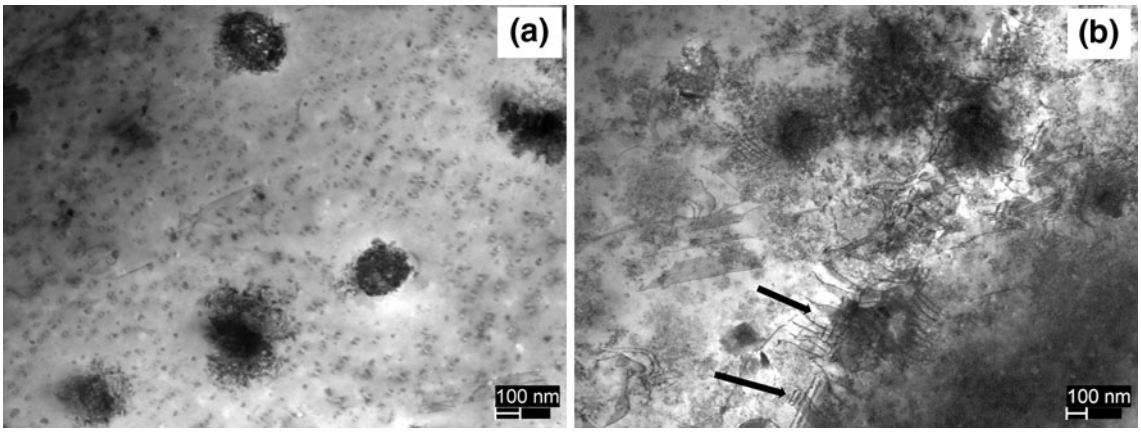

Fig. 9—STEM images from material hot rolled at 1000 °C show dislocations associated with precipitates in (*a*) and faulted dislocations in the vicinity of grain boundaries (indicated by the arrows) in (*b*).

as that at the higher rolling temperature. The proportion of low-angle (misorientation ≤5 deg) boundaries is actually less than that in material hot rolled at 1273 K (1000 °C). Also, the remainder of the distribution is still random. Refined grains containing annealing twins and peaks at 60 deg and 5 deg superimposed on otherwise random misorientation distributions were apparent at still lower rolling temperatures in the current work and have been previously reported throughout stir zones in materials subjected to FSP.

The representative micrographs obtained by STEM imaging of hot-rolled material are shown in Figure 9. Particles approximately 100 nm in size appear to be surrounded by dislocation tangles in Figure 9(a). The sizes and spacings of these particles are consistent with the κ_{iv} dispersion observed in Figure 7(b) and reported in Table II. Also observed in this image is a contrast effect at still finer precipitates, suggesting that coherent phase may be forming. At some locations, *e.g.,* as in Figure 9(b), faulted dislocations (indicated by arrows) seem to be emanating from a boundary. A moderate dislocation density was apparent throughout the transparent regions of the foils, although dislocation configurations varied significantly from location to location. In a TEM investigation of stir zone microstructures produced by FSP, subgrains approximately 1 to 2 μm in size were observed in the primary α at locations near the plate surface in contact with the tool shoulder. High peak temperatures in such locations resulted in grains 10 to 20 μm in size. Below the plate surface, primary α grains were refined to sizes of 1 to 2 μm and subgrains were no longer apparent. Dislocation spacings in the subgrain boundaries as well as subsequent OIM data suggest subgrain boundary misorientations of $\approx$1 deg.

The Al, Ni, and Fe components will contribute to solid-solution strengthening of the microstructure constituents in these NiAl bronze materials. The results of EDS measurement of concentrations of these elements in the primary α constituent and, separately, in the β transformation products are shown in Figure 10. All of these concentration measurements were made in materials that had been isothermally hot rolled to a 10:1 reduction, corresponding to an equivalent strain of 2.3. Such a strain and reheating between successive rolling passes to maintain isothermal conditions suggests that the concentration data in Figure 9 represent equilibrium concentration values for the constituents involved. Thus, the plots in Figure 10(a) represent the boundaries of the $\alpha+\beta$ two-phase field in the Cu-Al section of the Cu-Al-Ni-Fe quaternary diagram. Over the temperature range in these data, the solubility of Al decreases with temperature in both the α and β phases in a manner consistent with published data on NiAl bronzes. Likewise, the Ni and Fe partition between the α and β phases and the solubility of all of these solutes is evidently greater in the body-centered cubic structure of the β phase than in the face-centered cubic α phase.

IV. DISCUSSION

Altogether, the various microscopy data suggest that recrystallization during and immediately after the hot rolling results in a mainly annealed condition. The volume fractions of the primary α and the β-phase transformation products are temperature dependent, and dispersed phases are present in both of these constituents. The grain size in the primary α becomes finer at lower hot-rolling temperatures, and solute concentrations in both constituents are also temperature dependent. Dispersed particles were apparent in the primary α at 1273 K (1000 °C) or below 1173 K (900 °C), whereas dispersions are observed in transformation products of the β for all rolling temperatures.

A. *Estimation of the Ambient-Temperature Strength of Hot-Rolled Alloys*

During the thermomechanical processing in the current investigation, significant solute redistribution occurs in this multicomponent multiphase alloy depending on the temperature and duration of holding. It must also be recognized that the processing is not strictly isothermal and substantial solute partitioning and consequent microstructural changes may occur after completion of the processing operation and thus the

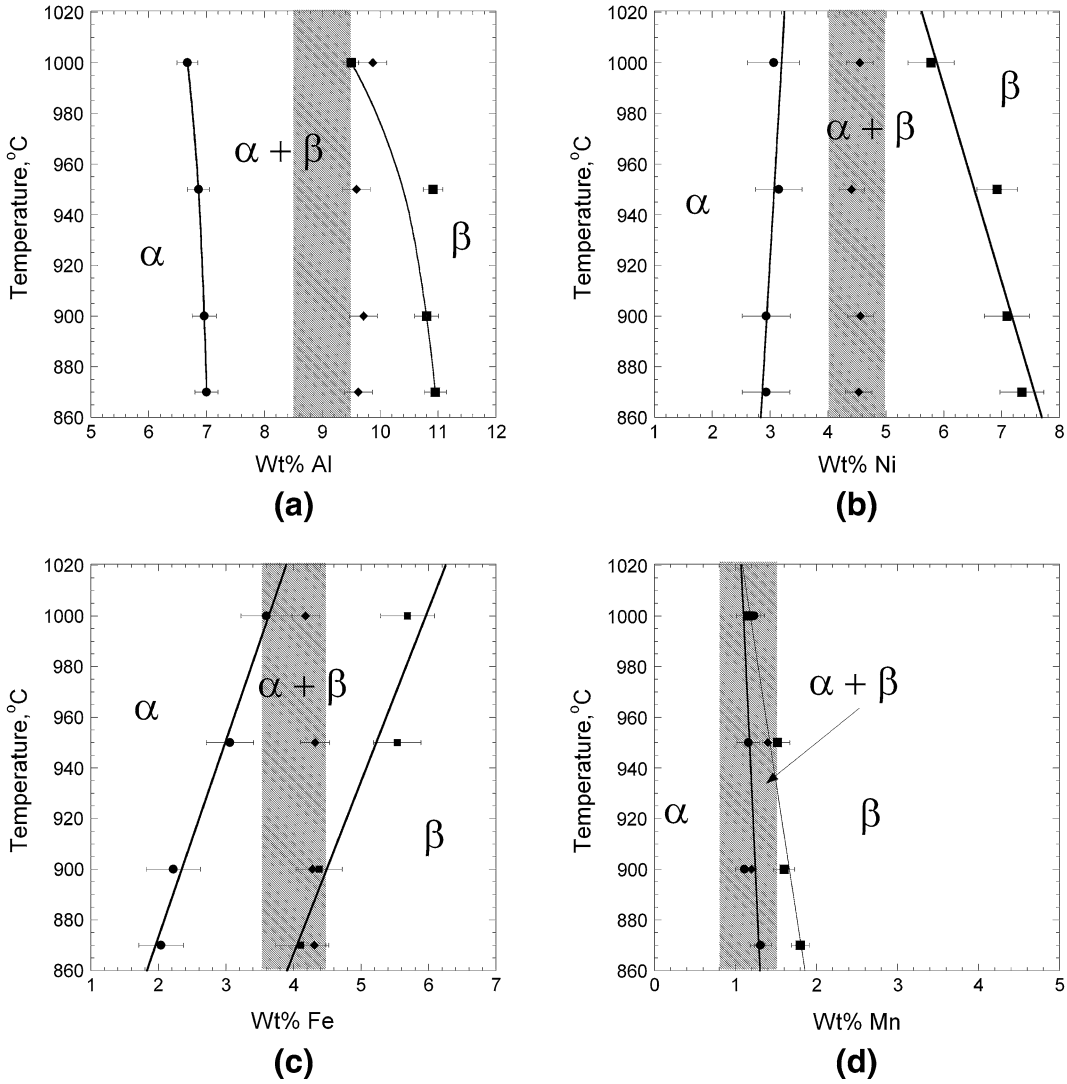

Fig. 10—EDS results obtained from materials hot rolled at various temperatures showing the phase boundaries in this Cu-Al-NI-Fe-Mn alloy. The shaded band reflects the composition limits for each of the alloy elements in this Cu-base alloy.

resulting microstructures as well as the mechanical properties reflect these changes. The volume fractions of the primary α and β-phase transformation products depend strongly on the hot-rolling temperature, and the overall yield strengthσ_{total} of the complex mixture of constituents, *e.g.*, as shown in Figure 2, is assumed to be described by an isostrain (rule of mixtures) model when loading parallel to the rolling direction, as follows:

$$\sigma_{\text{total}} = f_{\alpha}\sigma_{a} + f_{\beta}\sigma_{\beta} \quad [1]$$

where f and σ represent the volume fraction and yield strength of the primary α and the β transformation products. The necessary parameters required in such a rule of mixtures model are the mechanical properties and volume fractions of the individual phases.

Again, in this material the contributions to the yield strength of each of the constituents are assumed to be: (1) solid-solution strengthening; (2) strengthening caused by the grain size reduction in the α phase (as well as in the β transformation products) resulting from recovery, recrystallization, and grain growth occurring during and/or after the hot-rolling, as well as from phase transformations occurring in the β phase during cooling; (3) strengthening contributions from the various κ precipitate particles in both of the constituents; and finally, (4) strain hardening caused by dislocation structures remaining after cooling to ambient temperature. The strength of each of these α and the β phases can be described as

$$\sigma_{\alpha(\beta)} = \sigma_{\text{Solid solution}} + \sigma_{\text{Grain size}} + \sigma_{\text{Precipitation}} + \sigma_{\text{Dislocation}} \quad [2]$$

An evaluation of each of these strengthening contributions is described in the next section.

B. *Solid-Solution Strengthening in α and β*

The contribution of solid-solution hardening in these phases can be evaluated from the model proposed by

Fleischer[26] that expresses the critical resolved shear stress τ_c in the following form:

$$\tau_c \cong \frac{\mu}{700} \left|\eta' - \alpha\delta\right|^{3/2} c^{1/2} \quad [3]$$

where

$$\eta' = \frac{\eta}{(1 + 12|\eta|)}; \; \eta = \frac{1}{\mu}\left(\frac{\partial\mu}{\partial c}\right); \text{ and } \delta = \frac{1}{a}\left(\frac{\partial a}{\partial c}\right)$$

and where, in Eq. [3], α is 10 and 3 for edge and screw dislocations, respectively; δ is the misfit parameter; μ is the shear modulus (28.5 GPa for Cu-Al alloys[27]); a is the lattice constant (0.362 nm); and c is the solute concentration.

King[28] calculated the misfit parameter for numerous solid solutions and reported that the misfit parameter δ is +6.26 pct, –2.90 pct, and +1.50 pct, for Al, Ni, and Fe, respectively, in Cu. In the estimations of strength presented in this article, the separate solid-solution strengthening contributions from Al, Ni, and Fe are assumed to be additive. Lenkkeri and Lähteenkorva[29] determined the elastic moduli of Cu-Al solid solutions containing up to 16.6 at. pct Al and reported that η = –0.384. This value was used in the current work. Values of η' for the interaction of Ni and Fe are assumed to be 1, and all dislocations are assumed to be of the edge type.

Here, the solute concentration was determined by EDS analyses of the hot-rolled samples and averages of several measurements from the primary α and the β transformation products were used. Figure 10 shows the variation of the different solute concentrations in the constituents of this alloy as a function of temperature. These results illustrate the solute partitioning behavior in the Cu-Al-Ni-Fe-Mn system where no phase diagram data are currently available. The average elemental compositions as measured by EDS in this study are also shown in these plots, and the gray band delineates the allowed variation in composition for this alloy. A noteworthy feature of the data in Figure 10 is the rather steep phase boundaries of both the α and the β phases. Clearly, Al and Ni partition quite strongly between these phases while Fe shows very limited partitioning, and Mn seems to be rather uniform within experimental errors involved. Considering the low amount of Mn and the experimental errors, it is not possible to extract much information about the partitioning of Mn between the phases in this alloy. Interestingly, the Fe phase boundaries show that the solubility of Fe in both α and the β phases decreases with temperature. The solid-solution strengthening contributions in the α and the β phases were determined by using the experimentally determined phase compositions in Eq. [3].

C. *Grain Size Effects in α and the β Phases*

The yield strengthσ_y of a polycrystalline metal increases with refinement of the grain size d and the dependence is expressed by the well-known Hall-Petch[30,31] relation as

$$\sigma_y = \sigma_0 + kd^{-1/2} \quad [4]$$

where σ_0 is the intrinsic strength of the material in single crystal form, including solid solution (and thus varying with solute content) and dispersion strengthening contributions. The constant k is also dependent on solute content. Varschavsky and Donoso[27] have determined the grain size strengthening in several α-Cu-al alloys containing up to 19 at. pct Al (9.06 wt pct Al) and for a range of grain sizes. We have determined that $\sigma_0 = 27.5$ MPa and $k = 750$ MPa $\mu m^{1/2}$ from their results for a Cu-15 at. pct Al alloy, and thus, the solid-solution strengthening contribution in the primary α can be calculated. Although the solute concentration dependence of σ_0 and k is thus neglected, the errors involved are small especially because the variation in Al content of the alloys in this temperature range is only 6.67 to 7 wt pct (or 14.4 to 15.1 at. pct) as determined by EDS. The recrystallized grain size of the α phase (Table II) as measured from micrographs was used for the values of d.

The solid-solution strengthening in the β transformation products was approximately evaluated assuming that the Hall-Petch coefficients for this constituent were identical to those of the α phase containing 19 at. pct Al, and so they were calculated to be $\sigma_0 = 68.6$ MPa and $k = 705$ MPa $\mu m^{1/2}$ from Reference 27. The grain size within the β transformation products was obscured by phase transformations, and hence, d for this constituent was set to be that for the α phase. This assumption is not unreasonable because it seems that the bainite colony/packet size in, *e.g.*, Figure 7(a) is quite similar to the grain size of the α phase. An accurate measurement of this packet size was difficult because they were not always well defined.

D. *Precipitation Strengthening Contribution by κ Particles (lamellae) in α and β*

The yield strength of precipitation-hardened materials has been quite successfully predicted using Ashby's theory[32] so that the yield strength $\sigma_{Precipitation}$ may be taken as

$$\sigma_{Precipitation} = \frac{1.13\mu}{2\pi}\frac{b}{l}\ln\frac{2r}{r_0} \quad [5]$$

where b is Burgers' vector (0.256nm); r and l are the particle radius and spacing, respectively; and the adjustable parameter r_0 is taken as being equal to $4b$. Particle size and spacing values are included in Table II.

E. *Dislocation Density Contribution to the Strength*

An estimate of the contribution of the dislocation density to the strength was made using the relationship

$$\sigma_{Dislocation} = \alpha\mu b\sqrt{\rho} \quad [6]$$

where we take $\alpha = 0.5$ and ρ is the dislocation density. For subgrains ≈2 μm in size with boundary misorientations of ≈1 deg, the corresponding dislocation density

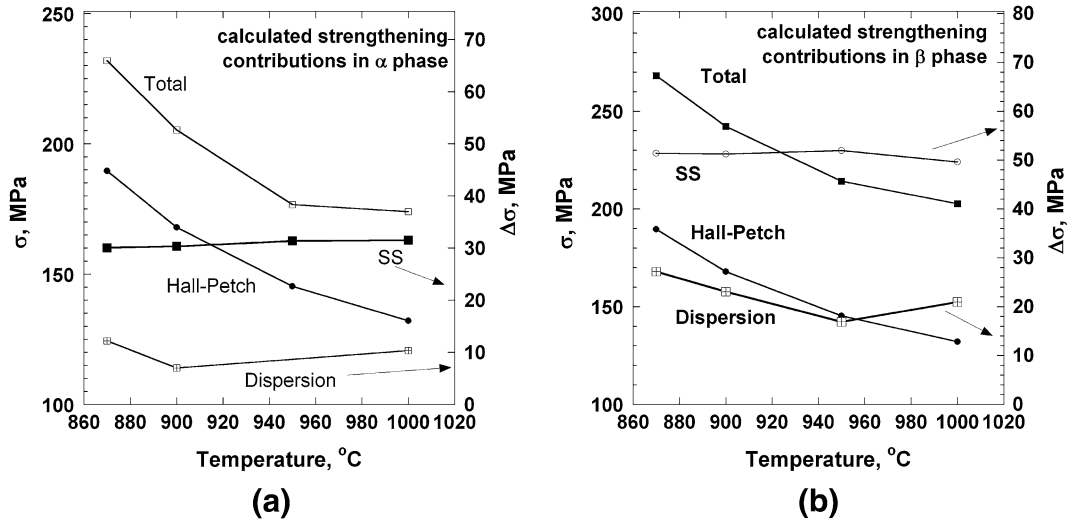

Fig. 11—Contributions to the yield strength of the separate constituents of this NiAl bronze alloy as calculated from the models of Eqs. [2] through [6]. It is noteworthy that the transformation products of β are always stronger than the primary α.

would be $\rho \approx 7 \times 10^{13}$ m^{-2}. Therefore, $\sigma_{\text{Dislocation}} \approx$ 30.2 MPa.

F. *Strengths of the Primary α and β Transformation Products*

From the foregoing, the alloy yield strength may be estimated by applying Eq. [1] after the strengths of the individual alloy constituents are computed using Eqs. [2] through [6], converting shear stress values to normal stress values where appropriate. The results for the individual constituents are shown in Figures 11(a) and (b). The contribution from solid-solution strengthening is not temperature dependent. The contribution from the dislocation density was assumed constant for this temperature range because the populations of low-angle boundaries in the misorientation distributions remained constant at approximately 0.15 for all hot-rolling temperatures. The grain size and precipitation terms reflect the stronger temperature dependence of the grain size as well as the size and spacing of the various precipitated phases. Considering the assumptions and approximations involved in these calculations as well as experimental errors, the plots in Figure 12 demonstrate good agreement between the alloy strength as calculated from Eq. [1] and the experimentally determined yield strength (Figure 6(a)). Of particular note is that the model predicts that the alloy yield strength will decrease relatively slowly with increasing hot-rolling temperature despite the more pronounced decreases in the yield strengths of the individual constituents.

G. *Application to the Strength in Stir Zones Produced by FSP*

A transverse section through the region of the initial passes after multipass FSP is shown in Figure 13. Overlap of the tool pin profile on adjacent passes during such multipass processing generally results in highly refined microstructures. However, some "uplift" of

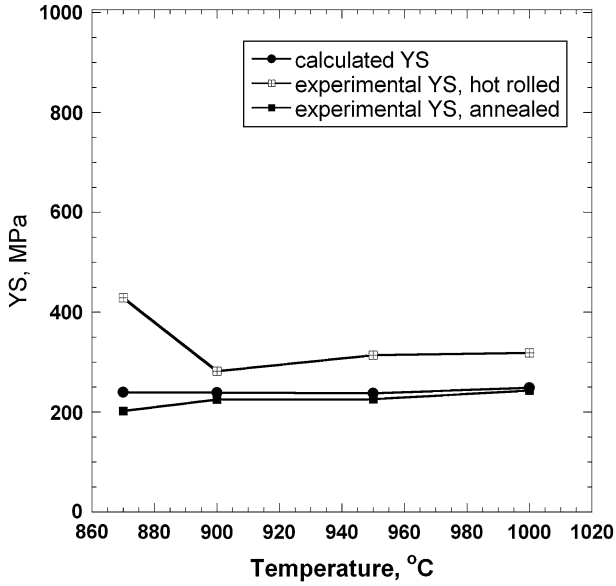

Fig. 12—The calculated yield strength for NiAl bronze material that has been annealed only or subjected to isothermal hot rolling at various temperatures is plotted as a function of temperature. The data of Fig. 11 were combined using Eq. [1] and the data of Fig. 4.

material from the base metal underneath the stir zone is discernable from the light–dark contrast near the center and at locations about 4.5 mm on either side of the centerline in Figure 13. Details of the microstructures at four locations below the plate surface in contact with the tool are shown in Figure 14. A comparison with the microstructures shown in, *e.g.*, Figures 2 and 3, reveals that the stir zone microstructures are generally finer than those produced by annealing along or by isothermal hot rolling. However, the results of tension tests of stir zone microstructures suggest a similar pattern to that observed in the hot-rolling experiments. Thus, stir zone locations nearby the tool shoulder apparently experience high local peak temperatures

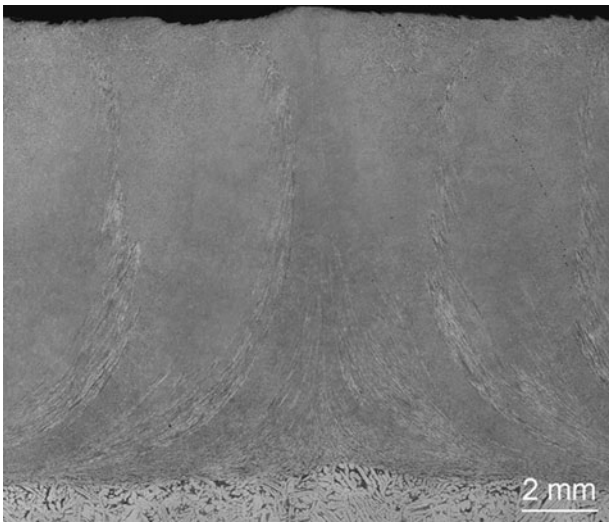

Fig. 13—A montage of optical micrographs shows a transverse section through the region of the initial passes in multipass friction-stir processing of alloy 2. The plate surface in contact with the tool is at the top of this image and the base metal microstructure may be observed at the bottom of the image. The uplift of base metal material in between adjacent passes may also be discerned in the stir zone formed by the processing.

approaching 1000 °C and develop larger fractions of β transformation products accompanying elongated, deformed primary α. Nevertheless, tensile ductility is also enhanced relative to the as-cast condition and may approach 30 pct throughout the stir zone.

Constituent compositions were evaluated as a function of depth below the plate surface in contact with the tool, and the results are depicted in Figure 15. These data were combined with measured grain size and precipitate dispersion parameters to predict the yield strength as a function of stir zone depth. In these calculations, the dislocation density term was taken to be the same as that estimated for the hot-rolled materials. The results of the calculated yield strength as a function of stir zone depth, shown in Figure 16, are compared with measurements made using miniature tensile samples machined from the stir zone. These miniature samples were machined with tensile axes either parallel to the local tool traversing (L2 samples) direction or transverse to this direction (T2 samples). Agreement between the calculated and measured yield strengths within the stir zone is excellent, and analysis of the various contributions to stir zone yield strength reveals that both grain size refinement and a high fraction of β transformation products results in the

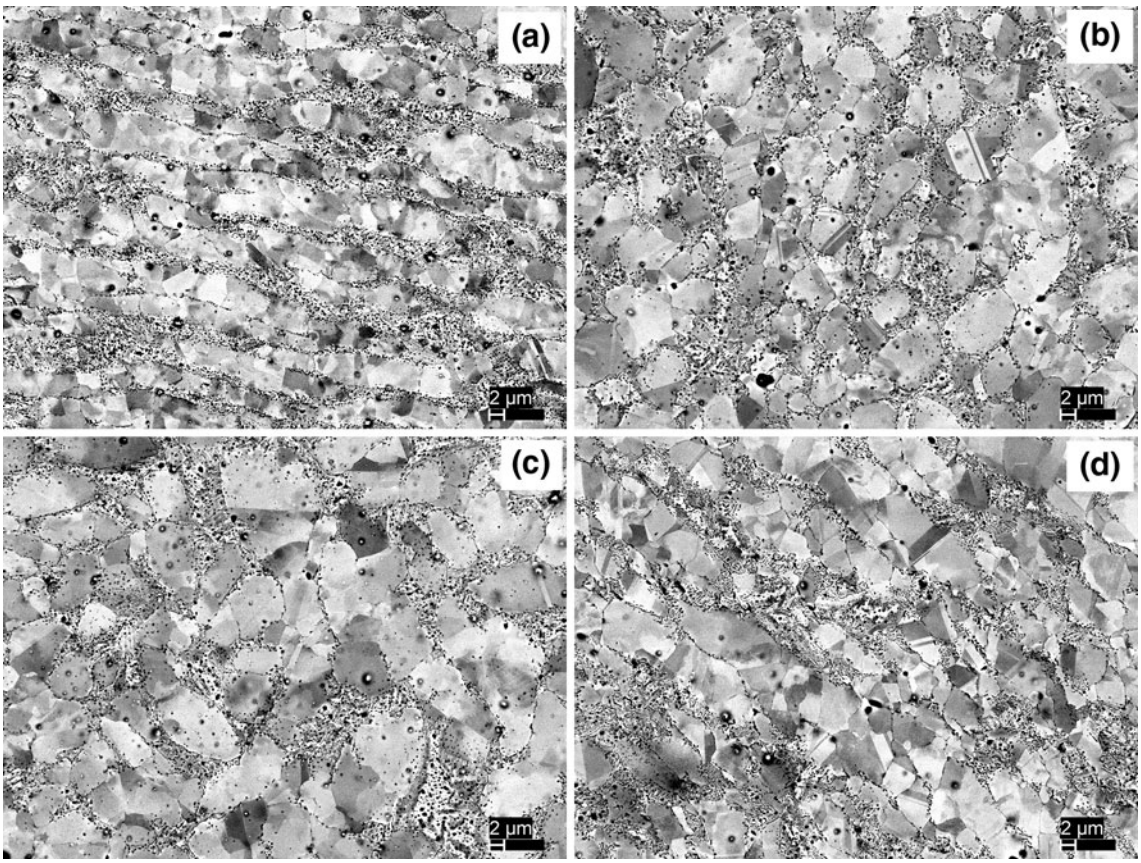

Fig. 14—Backscatter electron images from four positions at increasing depths below the plate surface in contact with the tool within the stir zone of Fig. 13 are shown here. (*a*) The depth below the surface is 200 μm, representing a location just under the surface. (*b*) The depth is 1 mm. (*c*) The depth is 5.5 mm. (*d*) The depth is 10 mm, *i.e.*, a location near bottom of the stir zone.

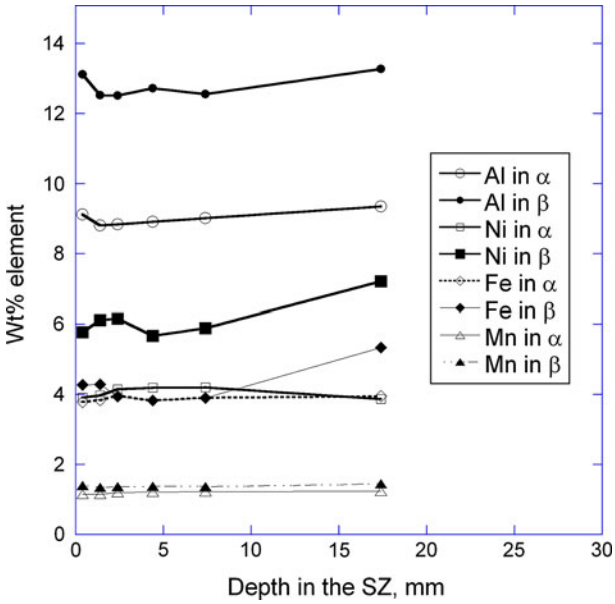

Fig. 15—EDS results for concentrations of Al, Ni, Fe, and Mn in both the primary α (open symbols) and in the transformation products of the β (closed symbols) as functions of depth in the stir zone of Figs. 13 and 14. These data enable the solid-solution contribution to the yield strength to be calculated as a function of stir position.

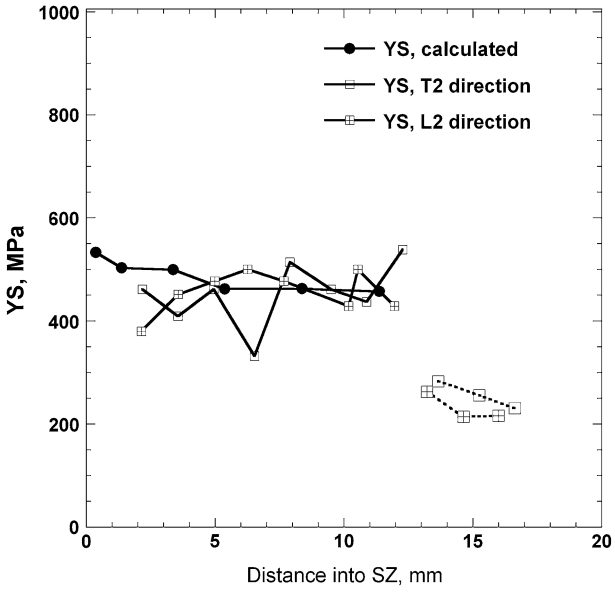

Fig. 16—The tensile yield strength as a function of stir zone depth for both longitudinal (L2) and transverse (T2) tensile samples is compared with the yield strength calculated by applying Eqs. [1] through [6] to experimentally determined solute content, grain size, dispersion parameters, and dislocation density values for this material. Agreement is excellent. These calculations were confined to the stir zone. The symbols corresponding to depths beyond 13 mm were measurements in the region below the stir zone.

increased strength of stir zone microstructures when a comparison is made to the hot-rolled materials.

Altogether, the results of this study suggest that high peak stir zone temperature accompanied by large strains during FSP will aid in producing high strength in combination with high ductility in the stir zone. This result is a consequence of microstructures consisting of large volume fractions of strong and ductile β transformation products during subsequent cooling after completion of FSP. Thus, FSP may be viewed as a potential method of surface hardening of cast NiAl bronze components while also enhancing ductility in processed regions. Finally, the modeling approaches developed in this study will be extended to consider the effects of gradients in microstructure, *e.g.*, as encountered at locations beneath the stir zone in Figure 13.

V. CONCLUSIONS

The following conclusions may be drawn from this investigation:

1. The hot rolling of NiAl bronze materials at temperatures above the eutectoid reversion reaction results in compatible deformation of the primary α and the β phases.
2. Recrystallization during and after rolling deformation produces refined and annealed grains in the primary α constituent.
3. Transformation in the β on cooling after rolling results in refined lamellar, particulate, and bainitic microstructures in the resulting transformation products.
4. The strengths of the two constituents can be described by and additive approach combining models for solid solution, precipitation, grain size, and strain hardening, and the alloy strength may then be predicted by combining terms for the individual constituents using an isostrain (rule of mixtures) approach.
5. Models for strengthening of hot-rolled material may also be applied without modification to predict yield strength *vs* depth in stir zones produced by FSP.
6. Such models may be applicable to assessing the role of microstructure gradients produced by FSP or other processes.

ACKNOWLEDGMENTS

The authors acknowledge support for this work under funding document N0001407WR20053 from the Office of Naval Research (ONR), with Dr. William Mullins as program monitor. S.S. acknowledges the support of the U.S. National Research Council (NRC) Research Associateship program.

OPEN ACCESS

REFERENCES

1. W.M. Thomas, E.D. Nicholas, J.C. Needham, M.G. Murch, P. Templesmith, and C.J. Dawes: G.B. Patent Application No. 9125978.8, Dec. 1991; U.S. Patent No. 5460317, 1995.
2. R.S. Mishra: *Adv. Mater. Process.*, 2003, vol. 161, pp. 43–46.
3. R.S. Mishra and Z.Y. Ma: *Mater. Sci. Eng. R*, 2005, vol. 50, pp. 1–78.
4. J.A. Schneider: *Friction Stir Welding and Processing*, R.S. Mishra and M.W. Mahoney, eds., ASM International, Materials Park, OH, 2007, pp. 37–49.
5. R.S. Mishra: *Friction Stir Welding and Processing*, R.S. Mishra and M.W. Mahoney, eds., ASM International, Materials Park, OH, 2007, pp. 309–50.
6. T.R. McNelley, K. Oh-Ishi, and A.P. Zhilyaev: *Friction Stir Welding and Processing*, R.S. Mishra and M.W. Mahoney, eds., ASM International, Materials Park, OH, 2007, pp. 155–73.
7. M.D. Fuller, S. Swaminathan, A.P. Zhilyaev, and T.R. McNelley: *Mater. Sci. Eng. A*, 2007, vol. A463, pp. 128–35.
8. K. Oh-ishi and T.R. McNelley: *Metall. Mater. Trans. A*, 2004, vol. 35A, pp. 2951–61.
9. K. Oh-ishi and T.R. McNelley: *Metall. Mater. Trans. A*, 2005, vol. 36A, pp. 1575–85.
10. J.-Q. Su, S. Swaminathan, S.K. Menon, and T.R. McNelley: *Metall. Mater. Trans. A*, 2011, vol. 42A, pp. 2420–30.
11. P. Weill-Couly and D. Arnaud: *Fonderie*, 1973, no. 322, pp. 123–35.
12. E.A. Culpan and G. Rose: *J. Mater. Sci.*, 1978, vol. 13, pp. 1647–57.
13. E.A. Culpan and G. Rose: *Br. Corros. J.*, 1979, vol. 14, pp. 160–66.
14. D.M. Lloyd, G.W. Lorimer, and N. Ridley: *Met. Tech.*, 1980, vol. 7, pp. 114–19.
15. P. Brezina: *Int. Met. Rev.*, 1982, vol. 27, pp. 77–120.
16. F. Hasan, G.W. Lorimer, and N. Ridley: *Proc. Intl. Conf. On Solid to Solid Phase Transformations*, TMS, Warrendale, PA, 1982, pp. 745–49.
17. F. Hasan, A. Jahanafrooz, G.W. Lorimer, and N. Ridley: *Metall. Trans. A*, 1982, vol. 13A, pp. 1337–45.
18. F. Hasan, G.W. Lorimer, and N. Ridley: *J. Phys.*, 1982, vol. 43, pp. C4 653–58.
19. A. Jahanafrooz, F. Hasan, G.W. Lorimer, and N. Ridley: *Metall. Trans. A*, 1983, vol. 14A, pp. 1951–56.
20. F. Hasan, G.W. Lorimer, and N. Ridley: *Metal Sci.*, 1983, vol. 17, pp. 289–95.
21. F. Hasan, J. Iqbal, and N. Ridley: *Mater. Sci. Tech.*, 1985, vol. 1, pp. 312–15.
22. G.W. Lorimer, F. Hasan, J. Iqbal, and N. Ridley: *Bri. Corros. J.*, 1986, vol. 21, pp. 244–48.
23. K. Oh-Ishi, A.P. Zhilyaev, and T.R. McNelley: *Metall. Mater. Trans. A*, 2006, vol. 37A, pp. 2239–51.
24. S. Swaminathan, K. Oh-Ishi, A.P. Zhilyaev, C.B. Fuller, B. London, M.W. Mahoney, and T.R. McNelley: *Metall. Mater. Trans. A*, 2010, vol. 41A, pp. 631–40.
25. J.K. Mackenzie: *Biometrika*, 1958, vol. 45, pp. 229–40.
26. R.L. Fleischer: *Acta Metall.*, 1963, vol. 11, pp. 203–09.
27. A. Varschavsky and E. Donoso: *Mater. Sci. Eng. A*, 1988, vol. A101, pp. 231–40.
28. H.W. King: *J. Mater. Sci.*, 1966, vol. 1, pp. 79–90.
29. J.T. Lenkkeri and E.E. Lähteenkorva: *J. Phys. F*, 1973, vol. 3, pp. 1781–88.
30. E.O. Hall: *Proc. Phys. Soc. B*, 1951, vol. 64, pp. 747–53.
31. N.J. Petch: *J. Iron Steel Inst.*, 1953, vol. 173, pp. 25–28.
32. M.F. Ashby: *Proc. Second Int'l Conf. on the Strength of Metals and Alloys*, ASM International, Materials Park, OH, 1970, pp. 507–41.